IEEE Robotics and Automation Letters (RA-L) paper, presented at ICRA 2026, Vienna, Austria. Cite as RA-L paper.

Suppressing Self-Excitation in Adaptive Sliding Mode Control: Observer-Based Design and Experimental Validation of Flapping-Wing Micro Aerial Vehicle

Heetae Park, Seungkeun Kim, and Jinyoung Suk

***Abstract*—This work covers the design of a sliding mode control to stabilize the attitude of a flapping-wing micro aerial vehicle. The approach employs an auxiliary observer loop to avoid system excitation from unmodeled actuator dynamics, a common issue in sliding mode control applications. A proportional-integral observer is constituted in the auxiliary loop to minimize interactions with the actuator dynamics and to handle parametric uncertainties in the low bandwidth. Then, the observer-based sliding mode control is designed to track the attitude command with the reconstructed state variables from the observer loop. Furthermore, a barrier function-based adaptive gain strategy is utilized to modulate the control input according to the system's current state, ensuring efficient use of control effort. Flight experiments were conducted with a freely movable dummy mass attached to the bottom of the vehicle, simulating external disturbances. The proposed sliding mode control outperforms proportional-derivative (PD), classical, and super-twisting sliding mode controllers in both tracking performance and control efficiency, while mitigating self-excitation due to discontinuous input.**

***Index Terms*—Aerial Systems: Mechanics and Control, Robust/Adaptive Control, Biologically-Inspired Robots**

I. Introduction

RECENTLY, flapping-wing micro aerial vehicles (MAVs) have drawn increasing attention due to their appealing features, such as hovering capability, agile maneuverability, and energy-efficient, silent flight. As relevant technologies mature, these vehicles are expected to handle increasingly complex applications in both indoor and outdoor environments. This growing demand also introduces challenges, including aggressive maneuvers, wind gusts, wing damage, carrying loads, perching, and collisions. Such undesirable conditions can be critical enough to degrade flight performance and stability, thereby necessitating the development of robust and adaptive control strategies that can ensure reliable behavior even in adverse environments.

Several control laws have been considered to control attitude in challenging circumstances [1]–[6]. For example, Kajak et al. [1] built a high-fidelity simulation model based on flight test data, successfully extending the flight regime from hovering to aggressive pitch maneuvers up to 70° through a gain-scheduled approach. Lee et al. [2] employed a nonlinear disturbance observer-based control, in which a nominal model was first learned in a disturbance-free environment using Gaussian Process Regression (GPR). The mismatch between the actual system response and the learned model was then used to identify and compensate for wind disturbances. Although previous approaches have demonstrated remarkable results, their performance strongly depends on the fidelity of the system model. Alternatively, sliding mode control (SMC) is preferred in environments where the system dynamics undergo substantial changes. In particular, SMC is highly effective under such conditions when integrated with adaptive control or an extended state observer [7]–[9]. By estimating disturbance torques and model parameters from the Lyapunov stability proof, it has been proved that the vehicles can be stabilized even in the presence of wind disturbances or wing damage [4], [6]. However, prior research does not use discontinuous control inputs or predetermine the switching gain to match the measured disturbance magnitude under abnormal conditions. As actuators can restrict the system bandwidth, the discontinuous input is typically approximated by the saturation function within a small range, referred to as the real sliding region. If the region is not appropriately set, the boundary layer approximation may lead to undesirable oscillations or divergence due to actuator delay. Hence, the region is com-

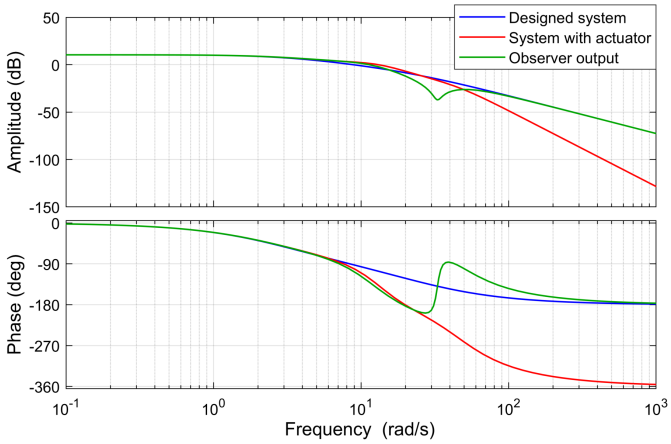

Fig. 1. System response with auxiliary observer.

Manuscript received: May, 22, 2025; Revised September, 9, 2025; Accepted October, 25, 2025.

This paper was recommended for publication by Editor Xinyu Liu upon evaluation of the Associate Editor and Reviewers' comments. This work was supported by Unmanned Vehicles Core Technology Research and Development Program through the National Research Foundation of Korea (NRF) and Unmanned Vehicle Advanced Research Center (UVARC) funded by the Ministry of Science and ICT, the Republic of Korea (2020M3C1C1A01084209).

All Authors are with the Department of Aerospace Engineering, Chungnam National University, South Korea skim78@cnu.ac.kr

Digital Object Identifier (DOI): see top of this page.

IEEE Robotics and Automation Letters (RA-L) paper, presented at ICRA 2026, Vienna, Austria. Cite as RA-L paper.

monly set to be sufficiently large to prevent the system from becoming unstable. This situation can result in a degradation in the overall performance, and especially in adaptive SMC, it can significantly impact stability when the system is excited by excessively increased gain.

This work introduces an adaptive sliding mode control with an auxiliary observer for roll and pitch stabilization of a flapping-wing micro aerial vehicle, aiming to preserve the inherent control performance while minimizing system excitation from unmodeled dynamics. As illustrated in Fig. 1, the underlying idea is to bypass the high-frequency discontinuous control to the observer loop to prevent system excitation, leading to the establishment of the sliding mode regardless of unmodeled dynamics [10]–[13]. Thus, the system can be free from the negative interaction between the unmodeled dynamics and adaptive gain, enabling it to fully leverage the benefits of discontinuous control. To this end, the barrier function–based adaptive gain is employed to alleviate the overestimation issue typically associated with adaptive gain. In addition, a proportional–integral (PI) observer is introduced to overcome the bandwidth limitations of conventional proportional observers: while fast poles are needed to cope with model uncertainties, actuator dynamics restrict such placement, leaving the system vulnerable. The integral channel compensates for these uncertainties without resorting to excessively high gains, thereby restoring robust estimation and improving overall closed-loop stability. This combined design recovers the degraded observation and control performance, enabling a more proactive response to observation errors while maintaining stability.

The article is organized as follows. Section II outlines the symbols used in this work. Section III presents the dynamics modeling of the flapping-wing micro aerial vehicle, while Section IV performs the stability analysis and design of the observer-based sliding mode control. Section V validates the performance of the proposed approach through flight experiments in a disturbed environment. Finally, Section VI concludes the article and briefly discusses directions for future research.

II. Notation

In this section, we introduce the main symbols and notations appearing in this work. Table I lists the key variables used for vehicle modeling.

TABLE I
List of Symbols

Symbol	Description
m, g	Mass and gravitational acceleration
u, v, w	Forward, lateral, and vertical body velocities
u_c, v_c, w_c	CoP velocities relative to the surrounding air
U, f	Wing speed and flapping frequency
θ, q, M	Pitch angle, pitch rate, and pitching moment
ϕ, p, L	Roll angle, roll rate, and rolling moment
I_x, I_y	Moments of inertia about roll and pitch axes
F_x, F_y, F_z	Body forces along the x-, y-, and z-axes
D_x, D_y, D_z	Drag forces along the x-, y-, and z-axes
T_f, T_r	Thrust forces from front and rear CoP
T_L, T_R	Thrust forces from left and right sides
δ_e, δ_f	Wing root deflection and differential flapping frequency
l_0, l_1	Distances from pivot point to CoP and from CoP to CoM
r_x, r_y	Distances from centerline to forward and lateral CoPs
b_f, b_r	Fore- and rear-instroke drag coefficients
b'_f, b'_r	Fore- and rear-outstroke drag coefficients
$b_{x,i}, b_{y,i}, b_{z,0}$	Drag coefficients along the x-, y-, and z-axes ($i = 0, 1$)

III. Vehicle description and modeling

A. Vehicle Description

The test vehicle used in this study is a tailless flapping-wing micro aerial vehicle featuring four wings, as shown in Fig. 2(a), with a wingspan of 45 cm and a mass of 120 g. Its four-wing design offers considerable benefits in vibration attenuation and propulsive efficiency, alleviating the inherent challenges of tailless configurations. In addition, the independent actuation of the bilateral wing pairs facilitates wing-based control through the modulation of wing kinematics. Specifically, control moments are generated by regulating flapping frequencies and wing twist distributions in the longitudinal and lateral directions, implemented through the dual flapping and control mechanisms. This design allows precise control over the vehicle's pitch, roll, and yaw, enabling stable hovering and a wide range of flight maneuvers. A more detailed explanation can be found in related work [14].

B. Longitudinal Model

As demonstrated in [1], [15], the simplified cycle-averaged model can effectively describe the dynamic characteristics in hover and slow maneuver flights, regardless of wing configurations. The overall model structure is represented in Fig. 3. The subsequent contents detail the development of the longitudinal model.

1) Rigid Body Dynamics: To model the cycle-averaged dynamics over one flap cycle, we assume that the change in moment of inertia due to the flapping motion is negligible and that the left and right wings are in phase. Then, the longitudinal equations of motion based on the body coordinates are represented as:

$$m(\dot{u} + \dot{\theta}w) = \Sigma F_x - mg\sin\theta, \tag{1}$$

$$m(\dot{w} - \dot{\theta}u) = \Sigma F_z + mg\cos\theta, \tag{2}$$

$$I_y\ddot{\theta} = \Sigma M. \tag{3}$$

2) Force and Moment Model: As shown in the free-body diagram in Fig. 2(c), the external forces can be classified into thrust and drag. For convenience in deriving equations, the center of pressure is distinguished by its location: the forward and backward places to consider respective thrust, while the central one accounts for drag. Then, the external forces and moment are given by:

$$\Sigma F_x = D_x, \tag{4}$$

$$\Sigma F_z = D_z - (T_f + T_r), \tag{5}$$

$$\Sigma M = -l_1 D_x + r_0(T_f - T_r). \tag{6}$$

IEEE Robotics and Automation Letters (RA-L) paper, presented at ICRA 2026, Vienna, Austria. Cite as RA-L paper.

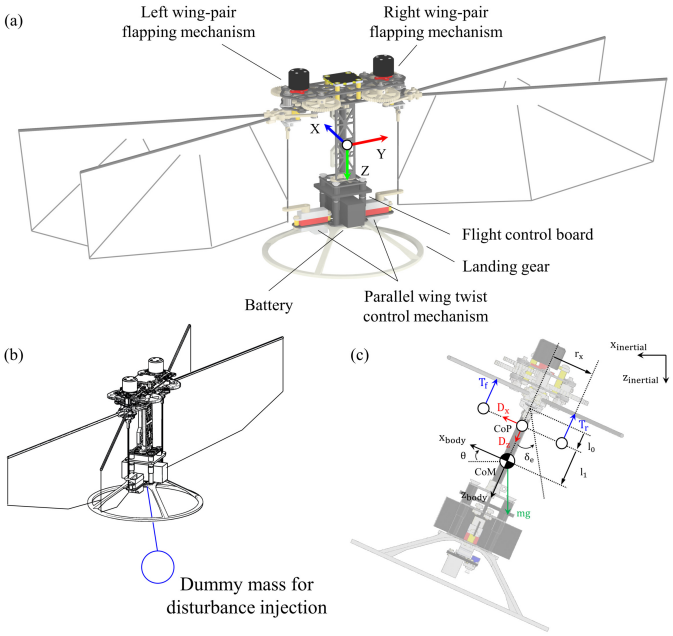

Fig. 2. (a) Overview of the flapping-wing micro aerial vehicle used in this work. (b) Experimental setups designed to apply dynamic disturbances. (c) 2D free-body diagram for longitudinal motion.

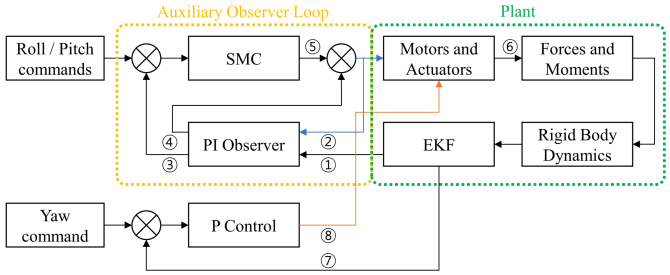

Fig. 3. Block diagram of the control system. ① Roll/pitch angle and angular rate, ② Commanded control input, ③ Observer state, ④ Integral control input, ⑤ Nominal control, ⑥ Real control input, ⑦ Yaw rate, ⑧ Yaw control.

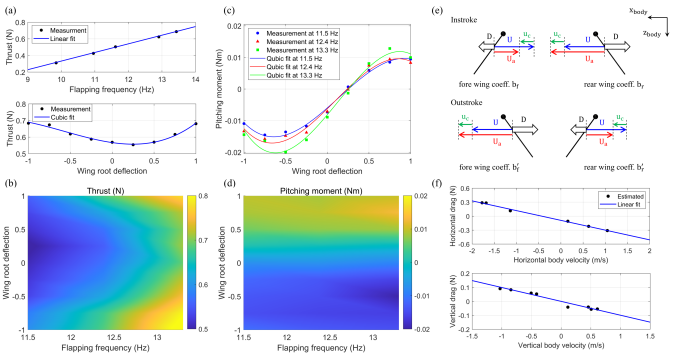

Fig. 4. Aerodynamic model constructed from experimental measurements: thrust (a)–(b), pitching moment (c)–(d), and drag (e)–(f). In (e), drag force is illustrated for the instroke and outstroke based on positive body velocity. The blue arrow indicates the wing speed at the center of pressure, the green one represents the body velocity in wing coordinates, and the red one portrays the relative wing speed.

Thrust is related to both the flapping frequency and the wing root angle, especially when employing the wing twist control. Here, the wing root angle is represented by a normalized deflection variable, defined as the wing root displacement divided by the maximum allowable deflection. To model thrust during hover, thrust was measured for a single pair of wings across various flapping frequencies and wing root deflection. The vehicle was mounted on a 3-axis load cell, which directly measured the forces along the body-frame x- and z-axes, as well as the pitching moment. Fig. 4(a) shows a linear dependence of thrust on flapping frequency within the flight regime, while indicating a quadratic trend with respect to the wing root deflection, where thrust increases at both low and high command levels. Accordingly, the thrust from a single wing pair is determined by flapping frequency and wing root deflection, as presented in Fig. 4(b). The thrust from both wing pairs in (5) is represented by: $T_f + T_r = 2T_{single}(f, \delta_e)$.

The corresponding pitching moment is also analyzed in Fig. 4(c), depending on the flapping frequency and wing root deflection. The moment varied linearly within the $\pm 50\%$ range, while a general decrease in control authority was observed beyond the range. Furthermore, the effect of flapping frequency on magnitude appears more prominently under negative wing root deflection. As a result, the pitching moment of a single wing pair is parameterized from the fitted surface shown in Fig. 4(d). The pitching moment from both wing pairs in (6) is modeled by: $r_0(T_f - T_r) = 2M_{single}(f, \delta_e)$.

The flapping-induced drag can be modeled from a linear damping model, assuming the angle of attack in the translational phase is constant and neglecting the rotational phase in stroke reversal. But, for our vehicle, the angle of attack during the stroke changes depending on the wing root angle δ_e because our wing-twist control regulates the wing tension and affects the angle of attack. To this end, the drag coefficient is defined according to the four stages of the stroke. Likewise, the wing speed and body velocity in the respective strokes are considered as indicated in Fig. 4(e). Near hovering flight, where the wing speed is much faster than the velocity of the center of pressure (CoP), the average drag on the instroke can be described as $\bar{D}_{in} = b_f(U - u_c)^2 - b_r(U + u_c)^2$, and on the outstroke can be written as $\bar{D}_{out} = -b'_f(U + u_c)^2 + b'_r(U - u_c)^2$. Then, the cycle-averaged horizontal drag force is expressed as: $D_x = 1/2(\bar{D}_{in} + \bar{D}_{out})$. Substituting $A = b_f + b'_r$ and $B = b'_f + b_r$, it simplifies to:

$$D_x = \frac{1}{2}(A - B)(U^2 + u_c^2) - (A + B)U u_c. \tag{7}$$

Note that the cycle-averaged horizontal drag force includes an additional nonlinear term $1/2(A - B)(U^2 + u_c^2)$, describing the force coefficient change associated with the wing root angle deflection. This model presents that the horizontal drag force is related to both the body velocity and wing root angle, and can even generate some drag force at zero body velocity, depending on the flight condition. Consequently, the variation of horizontal force with the wing root angle found in our earlier study can be explained through the model. To validate the drag model, we identified the drag forces via several flight experiments in near-steady conditions, where the translational accelerations and rotational angular velocity are near zero.

IEEE Robotics and Automation Letters (RA-L) paper, presented at ICRA 2026, Vienna, Austria. Cite as RA-L paper.

In those conditions, the drag forces are represented by the following equations:

$$D_x = mg\sin\theta, \tag{8}$$

$$D_z = T_f + T_r - mg\cos\theta. \tag{9}$$

The pitch angle and body velocities are obtained from motion capture cameras to ensure high accuracy, while the thrust is estimated from the thrust model in Fig. 4(a), with the measured flapping frequency. Fig. 4(f). indicates the body velocity-dependent drag force in both axes. The horizontal drag force model initially includes a nonlinear dependence on both the body velocity and the wing root deflection, reflecting the combined effect of body damping and changes in aerodynamic force due to wing twist change. Notably, the resulting cycle-averaged drag exhibits an approximately linear dependence on the body velocity, showing the negative force in zero body velocity. This suggests that the effective drag can be captured using a linear damping term despite the underlying nonlinear contributions. Moreover, the negative bias is consistent with our flight record, trimmed at a slightly negative pitch angle to maintain the hovering flight. Meanwhile, the vertical drag force is observed to be symmetrically linear to the body velocity. Thus, the drag coefficients in near-steady flight can be modeled as:

$$D_x = -b_{x,0}u_c - b_{x,1}, \tag{10}$$

$$D_z = -b_{z,0}w_c. \tag{11}$$

Considering the offset for the CoP and CoM, the velocities of the CoP relative to the surrounding air are described as:

$$u_c = u - l_1\dot{\theta}, \tag{12}$$

$$w_c = w. \tag{13}$$

C. Lateral Model

Following the same cycle-averaged modeling procedure, the lateral motion can be formulated with the body-axis lateral velocity, roll rate, and roll angle. Assuming negligible coupling with the longitudinal and directional motions, the lateral dynamics are written as

$$m\dot{v} = \Sigma F_y + mg\sin\phi, \quad I_x\ddot{\phi} = \Sigma L. \tag{14}$$

Analogous to the longitudinal case, the external forces in the lateral axis are dominated by the differential thrust and flapping-induced drag between the left and right wing pairs. The lateral force is modeled as:

$$\Sigma F_y = -b_{y,0}v - b_{y,1}, \tag{15}$$

where the damping coefficients are assumed to be identical to those identified for the longitudinal drag. The rolling moment is given by:

$$\Sigma L = r_y(T_l - T_r). \tag{16}$$

This formulation shows that the roll dynamics admit the same structure as the longitudinal model, with lateral drag and differential thrust governing the force and moment generation. Consequently, the control framework developed for pitch stabilization can be directly extended to the roll axis with only minor modifications in the state and input definitions.

D. Actuator Dynamics

The servo dynamic is modeled as a second-order system with a bandwidth of 50.54 rad/s and a damping ratio of 0.5, based on the identification results from related research [14]. Although the motor dynamic was not identified separately, it was modeled as a first-order system with a delay of 0.028 s, utilizing the results from [1].

IV. Flight control law

This section presents a control law formulated using a linearized model that focuses on longitudinal and lateral dynamics at hover, derived from the dynamics described in Section III. Although the servos and motors have been identified, actuator dynamics were treated as unmodeled in the observer design. Including actuator dynamics requires augmenting the observer with unmeasured actuator states, which in turn necessitates a higher observer bandwidth to accurately estimate those states. Such a high-bandwidth observer would be highly sensitive to the 12–13 Hz flapping motion, making estimation of actuator states impractical using attitude and angular rate measurements. Furthermore, incorporating actuator dynamics increases the system's relative degree, which requires higher-order derivatives in the sliding manifold and would significantly amplify noise in the feedback channel. Therefore, actuator dynamics are left unmodeled in control law design.

A. Stability Analysis

The basic structure of the observer-based sliding mode control is presented in Fig. 3, in which the observer loop is constructed as an ideal feedback loop. Nevertheless, the observer gain directly affects the stability of motion in sliding mode. The unmodeled dynamics related to the control bandwidth can especially restrict the observer gain. In this context, we describe the existence conditions of sliding motion and the sliding mode equation. Consider a linear time-invariant system and actuator dynamics.

$$\dot{x} = Ax + B\nu, \qquad y = Cx, \tag{17}$$

$$\dot{z} = A_z z + B_z\nu_{cmd}, \qquad \nu = C_z z. \tag{18}$$

where the system state is defined as $x = [u, q, \theta, v, p, \phi] \in \mathbb{R}^n$ with control input $\nu = [\delta_e, \delta_f] \in \mathbb{R}^m$. The output is $y \in \mathbb{R}^l$, and $z \in \mathbb{R}^p$ and $\nu_{cmd} \in \mathbb{R}^m$ denote the auxiliary state and control of the actuator dynamics. For implementation, the system is decomposed into longitudinal and lateral components, each equipped with a dedicated observer. Assuming that the system model is already represented in a regular form, the following conditions are satisfied:

$$x = \begin{bmatrix} x_1 \\ x_2 \end{bmatrix}, \quad A = \begin{bmatrix} A_{11} & A_{12} \\ A_{21} & A_{22} \end{bmatrix}, \quad B = \begin{bmatrix} 0 \\ B_2 \end{bmatrix}, \tag{19}$$

where $x_1 \in \mathbb{R}^{n-m}$ and $x_2 \in \mathbb{R}^m$. When the system model is not expressed in a regular form, it is necessary to first perform a nonsingular coordinate transformation to reformulate the system appropriately. The nonsingular coordinate transformation can be referred to [16]. Assuming the perfect model knowledge

IEEE Robotics and Automation Letters (RA-L) paper, presented at ICRA 2026, Vienna, Austria. Cite as RA-L paper.

and disregarding the actuator dynamics, the observer dynamics with the proportional-integral observer can be formulated as:

$$\dot{\hat{x}} = A\hat{x} + B\nu_{cmd} + L_p C(x - \hat{x}) - Bh, \tag{20}$$

$$\dot{h} = -L_i C(x - \hat{x}), \tag{21}$$

where $\hat{x} \in \mathbb{R}^n$ is the observer state, $h \in \mathbb{R}^m$ is the output integral error, and $L_p \in \mathbb{R}^{n\times l}$ and $L_i \in \mathbb{R}^{m\times l}$ are the proportional and integral observer gains, respectively. Then, the estimation error dynamics can be described by:

$$\begin{bmatrix}\dot{\tilde{x}}\\ \dot{h}\end{bmatrix} = \begin{bmatrix}A - L_pC & B\\ -L_iC & 0\end{bmatrix}\begin{bmatrix}\tilde{x}\\ h\end{bmatrix} + \begin{bmatrix}B\\ 0\end{bmatrix}(\nu - \nu_{cmd}). \tag{22}$$

where $\tilde{x} = x - \hat{x}$ is the estimation error. By defining the augmented state $\xi = \begin{bmatrix}\tilde{x} & h\end{bmatrix}^\top \in \mathbb{R}^{n+m}$, (22) can be rewritten as:

$$\dot{\xi} = A_\xi \xi + B_\xi(\nu - \nu_{cmd}), \tag{23}$$

$$\tilde{x} = C_\xi \xi, \tag{24}$$

where

$$A_\xi = \begin{bmatrix}A - L_pC & B\\ -L_iC & 0\end{bmatrix}, \quad B_\xi = \begin{bmatrix}B\\ 0\end{bmatrix}, \quad C_\xi = \begin{bmatrix}I & 0\end{bmatrix}.$$

A first-term $A_\xi\xi$ determines the stability of the estimation error dynamics, and a second-term $B_\xi(\nu - \nu_{cmd})$ arises from the discrepancy from the presence of the unmodeled actuator dynamics. Taking the Laplace transform of (23) - (24), while considering the actuator dynamics (18), results in:

$$\tilde{X}(p) = G_\xi(p)\Big(G_z(p) - I\Big)\nu_{cmd}(p), \tag{25}$$

where

$$G_\xi(p) = C_\xi(pI - A_\xi)^{-1}B_\xi, \quad G_z(p) = C_z(pI - A_z)^{-1}B_z,$$

and p is the Laplace variable. Regarding the stabilization problem, the sliding manifold with the observer state can be represented as follows:

$$\hat{s} = F\hat{x}. \tag{26}$$

Here, $\hat{s} \in \mathbb{R}^m$ is the sliding manifold and $F \in \mathbb{R}^{m\times n}$ is the manifold coefficient. Then, differentiating the sliding manifold with respect to time and substituting (20) gives

$$\dot{\hat{s}} = FA\hat{x} + FB\nu_{cmd} + FL_pC\tilde{x} - FBh. \tag{27}$$

Performing the Laplace transform to (28) and substituting (26) yields

$$p\hat{S}(p) - \hat{s}(0) = FA\hat{X}(p) - FBH(p) + W_o(p)\nu_{cmd}(p), \tag{28}$$

where

$$W_o(p) = FB + FL_pCG_\xi(p)\Big(G_z(p) - I\Big). \tag{29}$$

Since the analysis is conducted under the sliding motion, the initial condition term $\hat{s}(0)$ in (28) is omitted without loss of generality. If $W_o(p)$ is the non-minimum phase, the stability in sliding mode cannot be guaranteed because the equivalent control cannot be determined from the sliding motion $\dot{\hat{s}} = 0$. In that case, the equivalent control may have infinite or no solutions [17]. Therefore, to ensure stability in sliding mode, $W_o(p)$ should be the minimum phase to have at least one solution.

The overall system's stability can be further discussed if the equivalent control in sliding mode exists. As the sliding manifold converges to zero in sliding mode, (26) can be reformulated by decomposing $F = \begin{bmatrix}F_1 & F_2\end{bmatrix}$

$$F_1\hat{X}_1(p) + F_2\hat{X}_2(p) = 0, \tag{30}$$

where $F_1 \in \mathbb{R}^{m\times n-m}$ and $F_2 \in \mathbb{R}^{m\times m}$. Assuming $F_2 = I$ for simplicity and considering $\hat{X}(p) = X(p) - \tilde{X}(p)$ provides the following relation:

$$X_2(p) = -F_1X_1(p) + \begin{bmatrix}F_1 & I\end{bmatrix}\tilde{X}(p). \tag{31}$$

By using (31) and partitioning $FA = \begin{bmatrix}(FA)_1 & (FA)_2\end{bmatrix}$, the equivalent control input from (28) can be obtained as

$$\nu_{cmd,eq}(p) = -W_o^{-1}(p)\Big(FA\hat{X}(p) - FBH(p)\Big), \tag{32}$$

$$= -W_o^{-1}(p)\Big(E_xX_1(p) + E_\xi\xi(p)\Big), \tag{33}$$

where

$$E_x = (FA)_1 - (FA)_2F_1, \tag{34}$$

$$E_\xi = \begin{bmatrix}(FA)_2\begin{bmatrix}F_1 & I\end{bmatrix} - FA & -FB\end{bmatrix}. \tag{35}$$

Subsequently, the sliding mode equation can be represented by rearranging (17) using (19) and (31), and substituting the equivalent control (33) into (23).

$$\begin{bmatrix}pX_1(p)\\ p\Xi(p)\end{bmatrix} = A^*(p)\begin{bmatrix}X_1(p)\\ \Xi(p)\end{bmatrix}, \tag{36}$$

where

$$A^*(p) = \begin{bmatrix}A_{11} - A_{12}F_1 & \begin{bmatrix}A_{12}\begin{bmatrix}F_1 & I\end{bmatrix} & 0\end{bmatrix}\\ -N(p)E_x & A_\xi - N(p)E_\xi\end{bmatrix}, \tag{37}$$

$$N(p) = B_\xi\Big(G_z(p) - I\Big)W_o^{-1}(p). \tag{38}$$

Here, $\Xi(p) = \begin{bmatrix}\tilde{X}(p) & H(p)\end{bmatrix}^\top$ denotes the Laplace transform of the augmented state introduced in Section III.A. To assess the stability of the sliding mode, the characteristic equation can be examined as:

$$\det\Big(pI - A^*(p)\Big) = 0, \tag{39}$$

whose roots determine the system poles. In summary, the system is asymptotically stable provided that (i) $W_o(p)$ in (29) is minimum phase, (ii) the poles of the characteristic equation in (39) lie in the left half-plane, and (iii) the magnitude of the discontinuous control is sufficiently large compared to any external disturbances. A full proof of the stability of the observer-based sliding mode control can be found in [18].

B. Stability-Based Design

Given that stability conditions (i) and (ii) are satisfied, the observer gains can be designed by arbitrarily assigning the eigenvalues of the estimation error dynamics. In fact, the

IEEE Robotics and Automation Letters (RA-L) paper, presented at ICRA 2026, Vienna, Austria. Cite as RA-L paper.

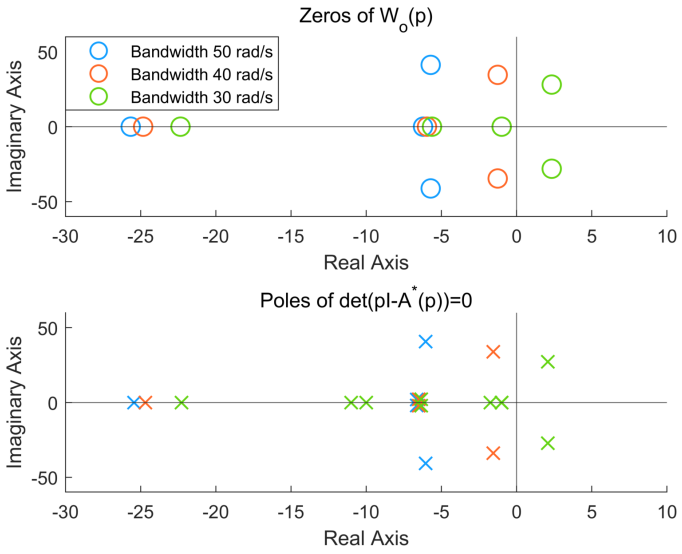

Fig. 5. Stability analysis within the sliding mode under different actuator bandwidths. As the actuator bandwidth decreases, the zeros of $W_o(p)$ gradually shift toward the right-half plane, which leads to the poles of $\det(pI - A^*(p))$ appearing in the right-half plane. This results in a loss of stability in the sliding mode.

observer gains can be classically designed such that A_ξ is Hurwitz by rewriting it in the following form.

$$A_\xi = \begin{bmatrix} A & B \\ 0 & 0 \end{bmatrix} - \begin{bmatrix} L_p \\ L_i \end{bmatrix} \begin{bmatrix} C & 0 \end{bmatrix}, \tag{40}$$

$$= A' - L'C'. \tag{41}$$

The output variables are set to the angles and angular rates in roll and pitch to stabilize the attitude. The observer poles are placed at $(-1, -9, -10, -10)$, representing a combination of slow and fast modes. While the pole at -1 is deliberately placed close to the origin to account for the integral action, the remaining fast poles are assigned to induce the proportional action. Specifically, the redundant pole at -10 serves to accumulate the integral error through the pitch rate error, rather than through the pitch angle. Fig. 5 illustrates stability conditions (i)-(ii) based on the placement of observer poles for unmodeled actuator bandwidths. As the bandwidth decreases, the stability deteriorates and becomes unstable at 30 rad/s. Although actuator bandwidth has a considerable impact on system stability, the designed control system remains stable even when the bandwidth is reduced by up to 20% from the identified performance (i.e., down to 40 rad/s), demonstrating robustness against moderate deviations in actuator bandwidth.

Typically, the discontinuous gain is selected to meet condition (iii), considering the bounds of external disturbances and model uncertainties, which are assumed to be unknown but bounded. However, accurately determining these bounds is not straightforward. If the gain is not properly set, it may result in actuator damage or failure to guarantee system stability. Therefore, it is desirable to avoid applying excessive input without compromising system stability. With this in mind, an adaptive gain based on a barrier function is employed, which preserves the sliding motion regardless of the disturbance magnitude once the sliding manifold is reached in finite time [19], [20]. The control input is represented as:

$$\nu_{cmd} = -M(\hat{s})\,\mathrm{sgn}(\hat{s}) + h, \tag{42}$$

where

$$M(\hat{s}) = \begin{cases} M_a,\ \dot{M}_a = \bar{M}\,|\hat{s}| & \text{if } 0 < t \le \bar{t}, \\ M_b = |\hat{s}|/\left(\epsilon - |\hat{s}|\right) & \text{if } t \ge \bar{t}. \end{cases} \tag{43}$$

The adaptive gain $M(\hat{s})$ consists of two phases. In the reaching phase, the gain evolves according to $\dot{M}_a = \bar{M}|\hat{s}|$, where $\bar{M}$ regulates the adaptation speed. In the sliding phase, the gain switches to $M_b = |\hat{s}|/(\epsilon - |\hat{s}|)$, where ϵ denotes the real sliding region. The reaching time $\bar{t}$ is defined as the time at which the sliding manifold reaches a small neighborhood of zero, specifically within $\epsilon/2$. The barrier function behaves similarly to a boundary layer approximation near the sliding region, effectively suppressing the chattering phenomenon. Additionally, an extra feedback h from the observer is included in the control input to compensate for accumulated estimation error, particularly when there is a significant deviation between the observer's state and the actual system response.

C. *Effect of Observer*

To further investigate the role of the observer, simulations were conducted with three configurations: a baseline SMC without an observer, an SMC with a Proportional (P) observer, and an SMC with a Proportional-Integral (PI) observer. To account for modeling uncertainties, the drag coefficient along the body x-axis, the aerodynamic center position, and the control moment magnitude were perturbed within $\pm 20\%$ of their nominal values. The results presented in Fig. 6 emphasize the critical function of the observer. Without an observer, the SMC exhibited self-excitation from the beginning of the flight due to the notch filter at the control input. The notch filter is designed to suppress the flapping-induced noise, but served as an unmodeled dynamic, similar to actuator dynamics, which destabilized the adaptive gain adjustment and led to persistent oscillations even after the external disturbance disappeared at 6 s. In contrast, both observer-based approaches successfully suppressed such excitations by compensating for the lost phase distortion. The PI observer also showed superior disturbance rejection, with its integral action enabling the states to converge rapidly to equilibrium.

A sensitivity analysis was conducted to evaluate the effect of different observer pole placements. Three pole sets were considered: a nominal set $(-1, -9, -10, -10)$, the fast set $(-1, -15, -16, -16)$ and a very fast set $(-1, -21, -22, -22)$. The phase portraits for the first 5 s after takeoff are shown in Fig. 7. The system exhibited persistent oscillations under the very fast set, with the angle fluctuating within $\pm 10^\circ$ and the angular rate within $\pm 150^\circ$/s. Although the nominal set maintained a relatively stable behavior, the response intermittently escaped from the sliding manifold after initially converging to it, even in the absence of external disturbances. In contrast, the fast pole set was found to offer a desirable balance, maintaining proximity to the sliding manifold with minimal oscillations. These results imply that

IEEE Robotics and Automation Letters (RA-L) paper, presented at ICRA 2026, Vienna, Austria. Cite as RA-L paper.

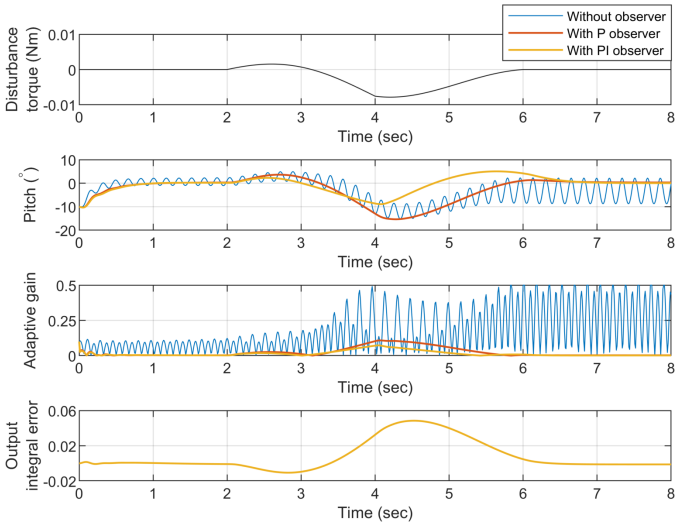

Fig. 6. Comparative analysis of control performance under different observer configurations: no observer, proportional observer, and proportional-integral observer.

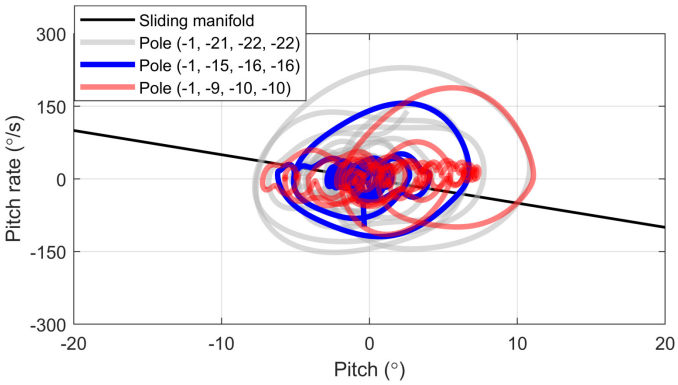

Fig. 7. Phase portraits for observer sensitivity analysis under three different pole placements.

TABLE II
SLIDING REGIONS USED IN THE FLIGHT EXPERIMENT

Axis	Classical SMC	Super-Twisting SMC	Proposed SMC
Roll	10	20	5
Pitch	5	10	2.5

the actuator dynamics in the real system may be slightly faster than those assumed in the model. Thus, the pole set $(-1, -15, -16, -16)$ was employed in the flight experiments as it showed the most desirable response.

V. RESULT AND DISCUSSION

To evaluate the performance of the designed control law under disturbance conditions, four control laws were compared: PD control, Classical SMC with barrier function, Adaptive Super-Twisting SMC [21], and the proposed SMC. The sliding regions for each method are summarized in Table II. Since the sliding manifold is defined as a linear combination of angular displacement and angular velocity, it is dimensionless. Hence, the sliding region can be interpreted as a tolerance band around the equilibrium state in the combined space of angle and angular velocity. The sliding region was slightly adjusted to account for the effects of the observer dynamics and the adaptive gain law. The angles and angular rates were provided to the observer based on estimates from the onboard extended Kalman Filter (EKF). As shown in Fig. 1(b), a 10 g dummy mass was attached beneath the vehicle to simulate dynamic disturbances. Each control law was evaluated over eight repeated trials. The flight tests included takeoff, hovering, forward/backward flight, and lateral flight. Fig. 8 illustrates the time-varying mean and standard deviation of the tracking errors, whereas Fig. 9 summarizes the root mean squared error (RMSE) and the corresponding control effort. The PD control exhibited minimal control effort and limited but acceptable tracking performance, with no noticeable oscillations. However, the pitch error converged relatively slowly, indicating limited responsiveness. In contrast, both the Classical SMC and the Adaptive Super-Twisting SMC produced persistent oscillations around 3–4 Hz across most axes, resulting in higher RMSE, standard deviation, and control effort. In particular, the Classical SMC and Adaptive Super-Twisting SMC frequently reached the actuator limits due to the slow response of the actuator. This observation suggests that self-excited SMC behavior can drive the control input from maximum to maximum, potentially causing actuator wear, failure, or reduced flight endurance. Meanwhile, the pitch response under Adaptive Super-Twisting SMC did not exhibit such oscillations, likely due to its relatively wide sliding region. As a result, the pitch variation increased after 6 s, implying limited disturbance rejection capability. On the other hand, the Proposed SMC did not show the 3–4 Hz oscillations and achieved the lowest RMSE and variation among all methods. Although its control effort was slightly higher than that of the PD control, it remained free from self-excited oscillations and substantially reduced the tracking error. This performance improvement is attributed to two key factors: (i) the use of an ideal observer model for feedback, which enables the adaptive gain to respond rapidly without delay, and (ii) the direct compensation of observer estimation errors within the controller, effectively preventing self-excitation. While the proposed method employs a PI observer, other observer types could also be integrated with adaptive gain laws. However, exceeding the actuator bandwidth in any observer design may lead to self-excitation in SMC regardless of the observer structure.

VI. CONCLUSION

In this work, we studied an observer-based adaptive sliding mode control for roll and pitch stabilization of a flapping-wing micro aerial vehicle. Conventional observer-based sliding mode controls perform well in handling unmodeled dynamics but are typically sensitive to parametric uncertainties or external disturbances. To address this issue, a PI observer was integrated into the control design to improve robustness. In addition, an adaptive gain based on a barrier function was incorporated to flexibly regulate the control input depending on the system's response. Experimental results demonstrated

IEEE Robotics and Automation Letters (RA-L) paper, presented at ICRA 2026, Vienna, Austria. Cite as RA-L paper.

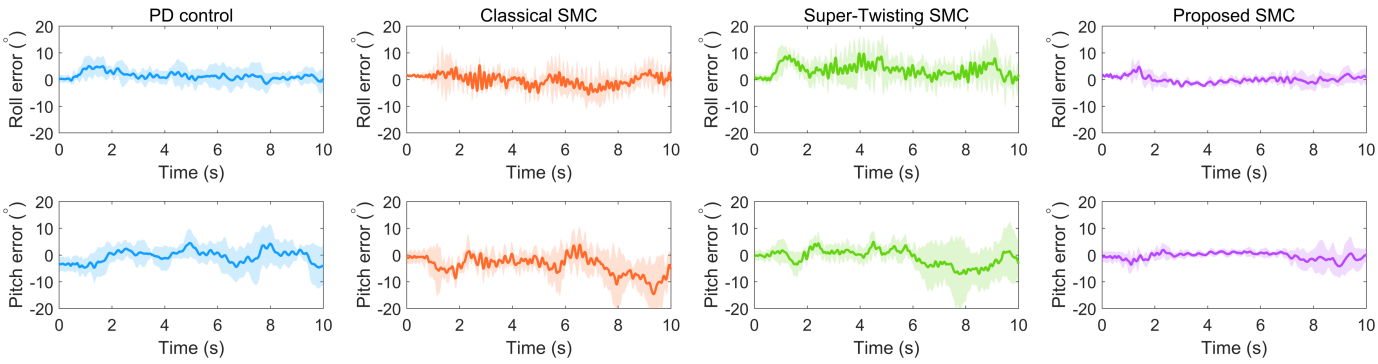

Fig. 8. Time series of roll and pitch tracking errors for different control laws. The solid lines represent the mean errors over multiple trials, and the shaded regions indicate ± 1 standard deviation.

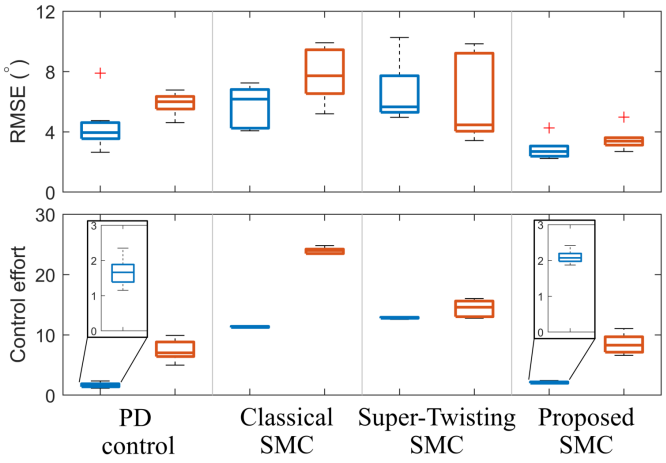

Fig. 9. Box plots comparing the root mean square error (RMSE) and control effort for different control laws. The control effort is defined as the root of the sum of squared control inputs over the flight duration.

that the proposed control law effectively stabilized the system even under rapidly acting disturbances, while suppressing self-excitation induced by the adaptive gain adjustment. In future work, we plan to compensate for the phase of the output error to more accurately estimate fast disturbances and to incorporate appropriate filtering into the observer to reduce the influence of high-frequency flapping motion.

REFERENCES

[1] K. M. Kajak, M. Karásek, Q. P. Chu, and G. C. de Croon, "A minimal longitudinal dynamic model of a tailless flapping wing robot for control design," *Bioinspiration & biomimetics*, vol. 14, no. 4, p. 046008, 2019.

[2] J. Lee, S. Ryu, and H. J. Kim, "Stable flight of a flapping-wing micro air vehicle under wind disturbance," *IEEE Robotics and Automation Letters*, vol. 5, no. 4, pp. 5685–5692, 2020.

[3] Z. Tu, C. Hui, L. Liu, Y. Zhou, D. R. Romano, and X. Deng, "Crawl and fly: A bio-inspired robot utilizing unified actuation for hybrid aerial-terrestrial locomotion," *IEEE Robotics and Automation Letters*, vol. 6, no. 4, pp. 7549–7556, 2021.

[4] P. Chirarattananon, K. Y. Ma, and R. J. Wood, "Adaptive control of a millimeter-scale flapping-wing robot," *Bioinspiration & biomimetics*, vol. 9, no. 2, p. 025004, 2014.

[5] Q. Guo, Z. Deng, C. Wu, F. Cui, Q.-H. Zhang, and J.-G. Lu, "Lpv modeling and robust sampled-data h_∞ control of a tailless flapping wing microaerial vehicle with parameter uncertainties," *IEEE/ASME Transactions on Mechatronics*, vol. 30, no. 2, pp. 1333–1344, 2025.

[6] Z. Tu, F. Fei, L. Liu, Y. Zhou, and X. Deng, "Flying with damaged wings: The effect on flight capacity and bio-inspired coping strategies of a flapping wing robot," *IEEE Robotics and Automation Letters*, vol. 6, no. 2, pp. 2114–2121, 2021.

[7] J. Hill, F. Fahimi, C.-k. Kang, and H. Aono, "Adaptive discrete-time sliding mode control applied to the pitch motion of a micro air vehicle with flapping wings," *Journal of Bionic Engineering*, pp. 1–11, 2025.

[8] A. Banazadeh and N. Taymourtash, "Adaptive attitude and position control of an insect-like flapping wing air vehicle," *Nonlinear Dynamics*, vol. 85, pp. 47–66, 2016.

[9] K. Bai, Y. Luo, Z. Dan, S. Zhang, M. Wang, Q. Qian, and J. Zhong, "Extended state observer based attitude control of a bird-like flapping-wing flying robot," *Journal of Bionic Engineering*, vol. 17, no. 4, pp. 708–717, 2020.

[10] V. Utkin, J. Guldner, and J. Shi, *Sliding mode control in electro-mechanical systems*. CRC press, 2017.

[11] K. D. Young, V. I. Utkin, and U. Ozguner, "A control engineer's guide to sliding mode control," *IEEE transactions on control systems technology*, vol. 7, no. 3, pp. 328–342, 1999.

[12] T. K. Vetter, "Sliding-mode control applied for robust control of a highly unstable aircraft," 2002.

[13] S. Wells and R. Hess, "Mimo sliding mode control for a tailless fighter aircraft, an alternative to reconfigurable architectures," in *AIAA Guidance, Navigation, and Control Conference and Exhibit*, 2002, p. 4650.

[14] H. Park, S. Kim, and J. Suk, "Tailless control of a four-winged flapping-wing micro air vehicle with wing twist modulation," *Bioinspiration & Biomimetics*, vol. 20, no. 2, p. 026005, 2025.

[15] S. B. Fuller, Z. E. Teoh, P. Chirarattananon, N. O. Pérez-Arancibia, J. Greenberg, and R. J. Wood, "Stabilizing air dampers for hovering aerial robotics: design, insect-scale flight tests, and scaling," *Autonomous Robots*, vol. 41, pp. 1555–1573, 2017.

[16] V. Utkin, A. Poznyak, Y. V. Orlov, and A. Polyakov, "Road map for sliding mode control design," 2020.

[17] V. I. Utkin, *Sliding modes in control and optimization*. Springer Science & Business Media, 2013.

[18] L. Hsu, J. P. V. Cunha, R. R. Costa, F. Lizarralde, E. V. L. Nunes, T. R. Oliveira, and A. J. Peixoto, "Nyquist criterion for chattering avoidance and global stability in observer-based sliding-mode control with parasitics," *Journal of the Franklin Institute*, vol. 361, no. 5, p. 106658, 2024.

[19] H. Obeid, L. M. Fridman, S. Laghrouche, and M. Harmouche, "Barrier function-based adaptive sliding mode control," *Automatica*, vol. 93, pp. 540–544, 2018.

[20] C. D. Cruz-Ancona, L. Fridman, H. Obeid, S. Laghrouche, and C. A. Pérez-Pinacho, "A uniform reaching phase strategy in adaptive sliding mode control," *Automatica*, vol. 150, p. 110854, 2023.

[21] Y. Shtessel, M. Taleb, and F. Plestan, "A novel adaptive-gain supertwisting sliding mode controller: Methodology and application," *Automatica*, vol. 48, no. 5, pp. 759–769, 2012.